Heterostructured Co/Mo-sulfide catalyst enables unbiased solar water splitting by integration with perovskite solar cells

Meng Wang, Zhi Wan, Xinying Meng, Zhihao Li, Xiaogang Ding, Pan Li, Can Li, Jian-Gan Wang [*], Zhen Li [*]

State Key Laboratory of Solidification Processing, Center for Nano Energy Materials, School of Materials Science and Engineering, Northwestern Polytechnical University and Shaanxi Joint Laboratory of Graphene (NPU), Xi'an 710072, PR China

ABSTRACT

Cost-effective and highly abundant oxygen evolution reaction (OER) electrocatalysts are of tremendous research interest in a variety of energy storage and conversion technology fields. However, the commercial applications are greatly impeded due to the sluggish OER kinetics. Herein, a heterostructured Co_9S_8 @MoS_2 electrocatalyst is demonstrated by elaborately implanting polyoxometalate of PMo_{12} into zeolitic imidazolate frameworks (ZIFs). The implantation of Mo species creates abundant Co_9S_8/MoS_2 hetero-interfaces that could fine-tune the electrocatalytic activity of cobalt sites and thereof enhance the OER activity. Density functional theory (DFT) results prove synergetic effects between Co_9S_8 and MoS_2 at the heterotinterfaces. The heterostructured Co_9S_8 @MoS_2 catalyst achieves a low overpotential of 242 mV to reach 10 mA cm^{-2} and the corresponding Tafel slope is as small as 58 mV dec^{-1}. Based on the superior OER activity, an unbiased solar water splitting system is built by integrating perovskite solar cell with the two-electrode Co_9S_8 @MoS_2//Pt/C, yielding a high solar-to-hydrogen (STH) conversion efficiency of 13.6%. This study demonstrates a new approach for cost-effective solar water splitting system toward green hydrogen production.

1. Introduction

Climate and energy crisis urge a fast transition from fossil energy to clean energy [1,2]. Hydrogen can be considered as an attractive alternative, which has high energy density and zero carbon emission [3–6]. Among the various hydrogen production methods, photovoltaic driven electrochemical (PV+EC) water splitting is a promising pathway due to the abundance of solar energy and high STH efficiency [7–10]. However, the PV+EC system is still limited in its use for hydrogen production due to the high material cost. Up to now, the benchmark water splitting catalysts are still noble metals like Pt and Ir/Ru oxides [11,12]. High cost, poor stability and scarce resource hinder their industrial applications. Thus, tremendous efforts have been focused on developing earth abundant electrocatalysts which have good durability and low cost for water splitting [13–17]. Perovskite solar cell (PSC) is an emerging solution process of PV technology with great potential to reduce the solar cell costs [18,19]. Integrating the earth abundant catalysts with low-cost PSCs opens a route toward cost-effective solar water splitting system [20–23].

During the electrolysis process of water splitting, OER is the efficiency-determining step owing to the multiple-electron process and kinetically sluggish [24–27]. Developing more efficient catalysts for OER is the key to increase the efficiency of overall water splitting. Among earth abundant OER catalysts, cobalt-containing catalysts show versatile catalytic properties due to the diverse chemical states of cobalt [28,29]. The local chemical environment near the cobalt sites strongly influences their catalytic properties [30,31]. To this end, heterostructured catalysts have been developed by combining cobalt with two or more metallic elements to improve the properties of cobalt sites. The heterostructures can achieve superior catalytic performance over those of the individual component through tuning the structural configuration. The interfaces in the heterostructures could provide more active sites and induce strong electronic interaction, thus to facilitate the adsorption of intermediates and effectively enhance the OER activity [32–36].

Metal- and covalent- organic frameworks (MOFs and COFs), in particular ZIFs, with high porosity, large surface area and flexible chemical composition, can be used as templates to synthesize Co-based

---

electrocatalysts [37–43]. At present, the common method to synthesize ZIFs derived bimetallic catalysts is partially replacing the Co^{2+} in the ZIFs with secondary metal ions, forming heterometallic ZIFs. The catalysts obtained through this method are usually with uniform composition. Such catalysts usually have serious agglomeration which is not conducive to electron transfer [44–47]. Besides, the metal ions incorporated in the ZIFs are limited by the metal coordination. Thus, it is highly desirable to obtain heterogeneous electrocatalysts with controllable morphology and composition from ZIFs precursors. PMo_{12} is a well-defined molybdenum metal-oxo cluster, which belongs to a class of polyoxometalates (POMs). The Co-containing ZIF-67 framework provides suitable cage size to accommodate guest species like PMo_{12} [48, 49]. In addition, the use of PMo_{12} can introduce secondary metal Mo, which is also regarded as an ideal element for catalysis due to its diverse chemical states [50]. Incorporation of PMo_{12} into ZIF-67 opens a route to synthesize ZIFs-derived heterostructured compounds which have effective coupling between the two transition metals.

Herein, we demonstrate a facile method to synthesize Co/Mo-sulfide electrocatalyst through sulfurization of the PMo_{12} @ZIF-67 precursor. A heterostructured catalyst with a structure of Co_9S_8 @MoS_2 is synthesized by controlling sulfurization temperature. The catalyst shows outstanding OER activity which needs an overpotential of 242 mV at 10 mA cm^{-2}. Moreover, an unbiased solar water splitting system can be built by integration a monolithic series-connected PSC with two-electrode Co_9S_8@MoS_2//Pt/C cell. The PSC-EC integrated system delivers a current density of 11.1 mA cm^{-2} without external bias for solar water splitting, achieving a high STH efficiency of 13.6%.

2. Experimental sections

2.1. Synthesis of precursor PMo_{12}@ZIF-67

Firstly, cobaltous nitrate hexahydrate (Co(NO$_3$)$_2$.6 H$_2$O) and phosphomolybdic acid hydrate (PMo_{12}) were dissolved in ultrapure water (molar ratio of Co:Mo=10:1) and stirred for 0.5 h to get solution A. 0.942 g 2-Methylimidazole was dissolved in anhydrous methanol and stirred until dissolved, than added slowly to solution A and stirred for 4 h. The resulting purple cloudy solution was then gathered by centrifuging, and washed three times with ultrapure water and absolute ethanol. At last, the obtained purple precipitates were dried at 60 °C overnight under vacuum. The synthesis of ZIF-67 was conducted using the same synthetic process only with addition of Co(NO$_3$)$_2$.6 H$_2$O.

2.2. Synthesis of CoMoS-x

The obtained PMo_{12} @ZIF-67 and thiourea were put into a porcelain boat with a mass ratio of 1:8. The thiourea was placed at the upstream. Then heat the porcelain boat to 500/750/850 °C for 120 min in a flowing Ar atmosphere to obtain the corresponding CoMoS-X samples. Co_9S_8 and MoS_2 were obtained by sulfurization of only ZIF-67 and PMo_{12}.

2.3. Characterization

The morphology of the catalysts was obtained through scanning electron microscope (SEM) on the Nova NanoSEM 450 (FEI). The microstructure of the catalysts was obtained through transmission electron microscopy (TEM) on the JEM-2100 F (JEOL). The chemical compositions were obtained by X-ray photoelectron (XPS) spectra on the Kratos AXIS spectrometer (Shimadzu). The crystalline structures of the samples were obtained by X-ray diffraction (XRD) using the XRD-6000 diffractometer (Shimadzu). The ultraviolet photoemission (UPS) spectra were performed using the ESCALAB 250Xi spectrometer (Thermo Scientific). Fourier-transform infrared spectra (FTIR) were conducted using the spectrometer of Nicolet 6700 (Thermo Scientific). The Raman spectra were carried out using a Renishaw inVia. The atomic

contents of catalysts were characterized by ICP-OES (Agilent 5110).

2.4. Electrochemical tests

To prepare the working electrodes, the catalyst powders were grinded and dissolved in the solution containing Nafion, ethanol and water, followed by sonication to get a homogenous ink solution. Then the ink solution was added on the hydrophilic carbon cloth to get the working electrode (loading: 0.3 mg cm^{-2}).

The electrochemical OER activity of all samples was tested with a three-electrode system on a Chenhua CHI 760E workstation. A Pt plate (1 cm^2) was employed as counter electrode and a saturated Ag/AgCl was employed as reference electrode. The electrolyte was freshly prepared KOH solution with the concentration of 1.0 M. The potentials measured can be converted to reversible hydrogen electrode (RHE) as:

$$E\ (RHE) = E\ (Ag/AgCl) + 0.197\ V + 0.059\ pH\cdot$$

All polarization curves were carried out with iR compensation at the scan rate of 10 mV s^{-1}. The value of electrochemical double-layer capacitance (C_{dl}) can be obtained through cyclic voltammetry (CV) curves at various scan rates, and electrochemically active surface area (ECSA) is calculated as below:

$$ECSA = C_{dl}/C_s$$

Where C_s is 0.04 mF cm^{-2} under alkaline condition. Electrochemical impedance spectroscopy (EIS) tests were recorded at 1.53 V vs. RHE, and the frequency range is from 1000 Hz to 0.01 Hz.

For two-electrode water splitting test, Co_9S_8 @MoS_2 anode coupled with Pt/C cathode was used. Under chopped illumination of simulated AM 1.5 G, the current of PSC driven water splitting without applying an external bias was recorded by chronoamperometry. The active area of monolithic series connected PSC device was 0.8 cm^2, and the area of the catalyst electrode was 1 cm^2. The efficiency of STH is calculated as:

$$\eta STH = \frac{J\ \ (mA\ \ cm^{-2}) \times 1.23\ \ V}{P\ \ (mW\ \ cm^{-2})}\ \ \times 100\%$$

where J represents the operating current density in PSC-EC integrated system at zero bias under illumination, 1.23 V represents the theoretical voltage value to drive water splitting, P indicates the power density of the simulated solar incident light, which is 100 mW cm^{-2}.

3. Results and discussion

3.1. Characterizations

Fig. 1 illustrates the procedures for the synthesis of target Co/Mo-sulfides. The self-assembly of ZIF-67 was performed at the presence of PMo_{12}. SEM images in Fig. 2a and b indicate that the PMo_{12} @ZIF-67 hybrid perfectly preserves the polyhedral morphology of the ZIF-67. The rougher surface and increased particle size of the PMo_{12} @ZIF-67 are mainly due to the incorporation of PMo_{12}. XRD peaks from both PMo_{12} and ZIF-67 can be identified in the PMo_{12} @ZIF-67 hybrid (Fig. S1a). FTIR spectrum of the PMo_{12} @ZIF-67 hybrid (Fig. S1b) appears two additional absorption peaks at 867 and 939 cm^{-1}, which belong to Mo-O and Mo=O [51]. These results confirm the successful introduction of PMo_{12} species into the ZIF-67 matrix during the self-assembly process without compromising the framework structure.

The PMo_{12} @ZIF-67 precursor was then sulfurized by thiourea at high temperatures to attain the desired Co/Mo-sulfide catalysts. The sulfurization temperature is an important factor which can influence the electrocatalytic properties of the Co/Mo sulfides. Thermogravimetric analysis (TGA) was conducted in Ar as shown in Fig. S2. PMo_{12} @ZIF-67 shows a moderate mass loss when the temperature is below 500 °C, which is likely due to removal of guest water and weakly linked 2-MeIm in the ZIF-67, accompanying by the decomposition of PMo_{12}. As the
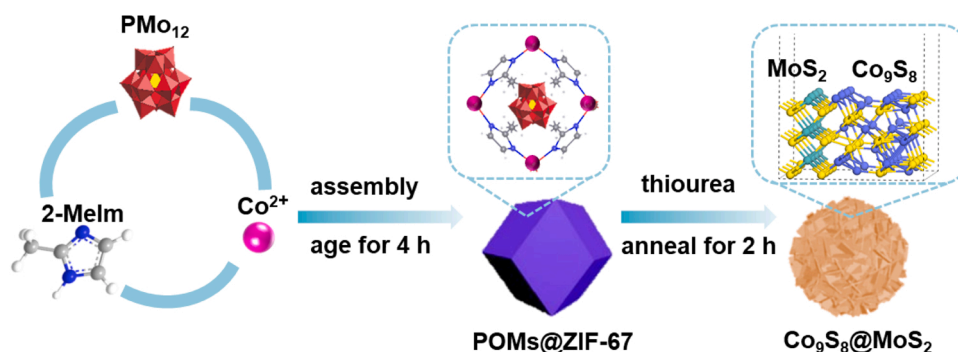
Fig. 1. Schematic illustration for the fabricated procedure of PMo_{12} @ZIF-67 precursor and Co/Mo-sulfide electrocatalyst.
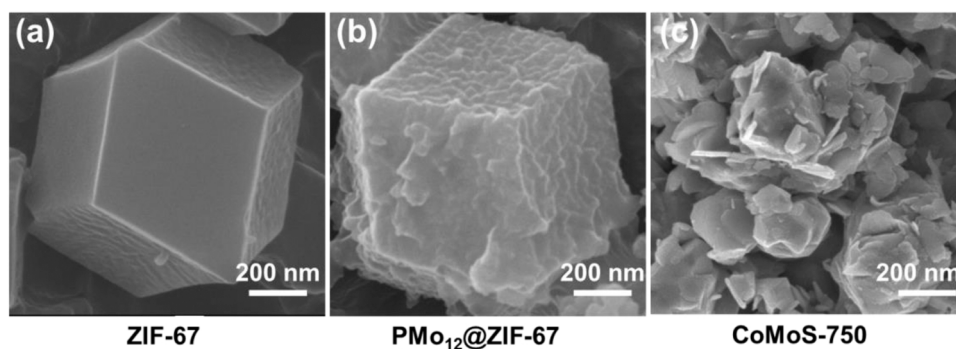

Fig. 2. SEM images of the (a) pure ZIF-67, (b) PMo_{12} @ZIF-67 precursor and (c) CoMoS-750.

temperature increases to over 500 °C, both PMo_{12} @ZIF-67 and ZIF-67 show sharp mass decline, indicating the collapse of the MOF frameworks [52]. The collapse of MOF framework is expected to generate abundant heterogeneous interfaces with bimetallic reactive sites. According to the OER performance of catalysts with different sulfurization temperatures mentioned later in the paper, 750 °C was chosen as the sulfurization temperature. For easy annotation, the catalyst sulfurized at 750 °C is denoted as CoMoS-750 in the following discussion.

Fig. 2c shows the representative SEM image of the CoMoS-750 catalyst. The morphology of the catalyst changes dramatically after sulfurization. Nanosheets are formed on the outside of catalyst. Fig. 3a gives the phase structure of CoMoS-750 analyzed by XRD. The diffraction peaks for Co_9S_8 (JCPDS: 19–0346) and MoS_2 (JCPDS: 17–0744) are fully matched. The Raman spectroscopy was further characterized to explore the structure of CoMoS-750 catalyst (Fig. 3b). The Raman bands at 283, 376, 403 and 447 cm^{-1} can be assigned to the MoS_2 [53]. The

peaks at around 190, 500 and 670 cm^{-1} can be assigned to Co_9S_8 [54]. Based on these results, the CoMoS-750 catalyst is consisted of a heterostructure with MoS_2 and Co_9S_8. As mentioned above, the product obtained is related to the sulfurization temperature. For comparison, we also tested the XRD and Raman spectra of CoMoS-500, as show in Fig. S3. A double metal sulfide of $CoMoS_4$ @CoS_2 is obtained with sulfurization at 500 °C. When the sulfurization temperature is gradually increased to 750 °C, the amorphous $CoMoS_4$ can be converted to crystalline MoS_2, accompanied by the phase transformation of cobalt sulfide from CoS_2 to Co_9S_8.

TEM was conducted to further characterize the microstructure of the catalyst. As given in Fig. 4a, the catalyst presents a unique heterostructure, where the nanosheet shell wraps the polyhedral core. Fig. 4b illustrates the high-resolution TEM (HRTEM) image of the catalyst. A lattice spacing about 0.61 nm is resolved, well matching to the interlayer distance of the MoS_2 (002) planes [55]. The lattice spacings about
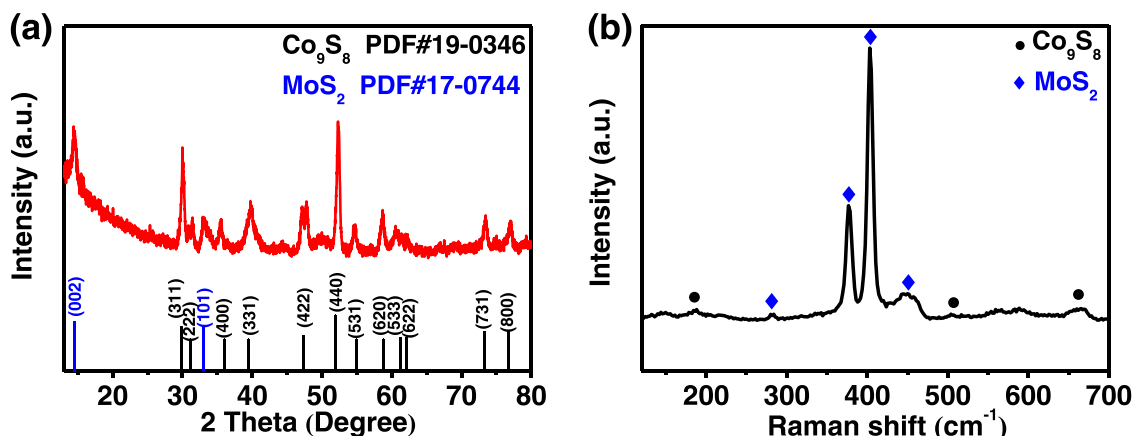

Fig. 3. (a) XRD diffractions and (b) Raman spectrum of CoMoS-750 catalyst.
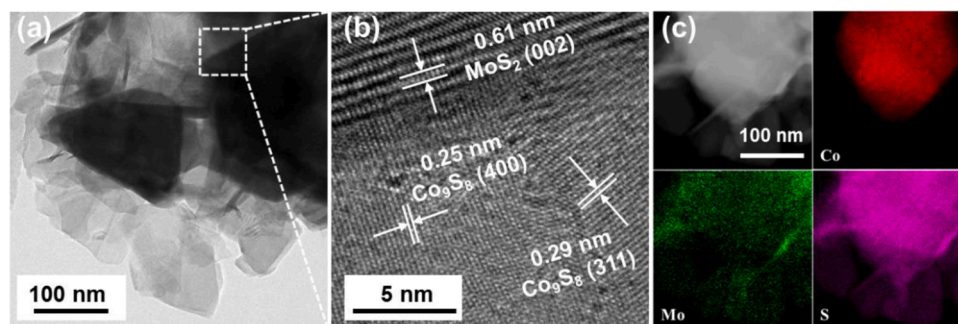
Fig. 4. TEM characterizations of the heterostructure of CoMoS-750 catalyst. (a) TEM, (b) HRTEM and (c) EDS elemental mapping images of the CoMoS-750 catalyst.

0.29 and 0.25 nm at the internal core belong to the Co_9S_8 (311) and Co_9S_8 (400) planes [56,57]. The heterogeneous interfaces between the MoS_2 and the neighboring Co_9S_8 can be resolved in the HRTEM image. The intimate contact could introduce strong electronic interactions and facilitate charge transfer, which is favorable for enhancing the catalytic activity [58]. EDS mapping reveals the element distribution (Fig. 4c). It can be found that Co mainly locates at the interior of the catalyst, while Mo and S uniformly distribute in the whole catalyst, which is in consist with the Co_9S_8 @MoS_2 heterostructure revealed by HRTEM. ICP-OES results indicate that the atomic ratio of Mo/Co/S is ca. 1:3.7:5.5.

The chemical states of the obtained electrocatalysts were investigated through XPS tests. Fig. S4 gives the full elemental survey, suggesting that the catalyst contains elements of Co, Mo, C, O and S. The detailed spectrum of Co 2p is presented in Fig. 5a. Two pairs of spin-orbit doublet peaks are observed along with two shakeup satellite peaks. A peak at 793.8 eV belongs to Co^{3+} $2p_{1/2}$ and peak at 778.7 belongs to

Co^{3+} $2p_{3/2}$. Another two peaks located at 796.6 and 780.9 eV belong to $2p_{1/2}$ and $2p_{3/2}$ of Co^{2+} [59]. Fig. 5b presents the Mo 3d spectrum. The peaks located at 229.0 and 232.2 eV can be assigned to Mo^{4+} $3d_{5/2}$ and Mo^{4+} $3d_{3/2}$. A peak of S 2 s can be found at 226.7 eV. In addition, a pair of peaks with low intensity appear at 233.2 and 235.6 eV correspond to the Mo^{6+} $3d_{5/2}$ and Mo^{6+} $3d_{3/2}$ [60], which may be caused by the partially oxidation of the surface MoS_2. As for XPS of S 2p in Fig. S5, two peaks at 163.0 and 161.7 eV can be attributed to S 2p [61], corresponding to the chemical valence state of S^{2-} in the MoS_2. In addition, Fig. 5a and b compare the binding energies of Co and Mo in the heterostructured catalyst with the pure Co_9S_8 and pure MoS_2. The peaks of Co 2p are shifted positively, while the Mo 3d peaks are shifted to negative energy. This suggests that there is an electronic interaction between Co_9S_8 and MoS_2 in heterostructured catalyst, resulting in electron transfer from Co_9S_8 to MoS_2.

UPS was applied to characterize the energy levels of Co_9S_8 and MoS_2
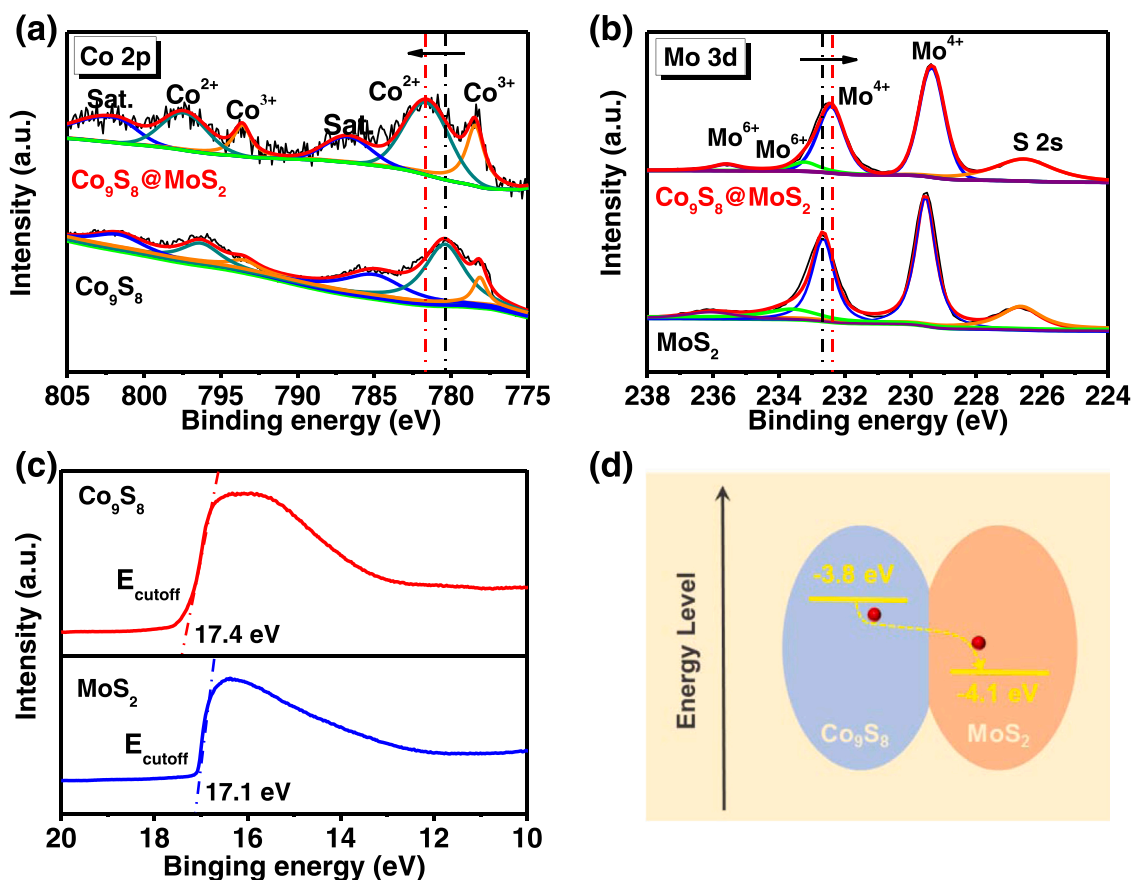
Fig. 5. Chemical and energy level of the Co_9S_8 @MoS_2, Co_9S_8 and MoS_2. XPS spectra of (a) Co 2p and (b) Mo 3d for heterostructured Co_9S_8 @MoS_2 and pure MoS_2. (c) UPS spectra of the Co_9S_8 and MoS_2. (d) Energy-level diagram of MoS_2 and Co_9S_8.

(Fig. 5c). The Fermi level (E_F) position can be attained using $E_F = E_{cutoff}$ - 21.2 eV from the cutoff energy (E_{cutoff}) illustrated in Fig. 5d. The E_F of MoS_2 and Co_9S_8 are 4.1 and 3.8 eV (relative to the vacuum level), respectively. The energy difference prompts electron transfer from Co_9S_8 to MoS_2, and this result is in align with XPS. Electron transfer between Co_9S_8 and MoS_2 would modulate the catalytic properties of the heterostructured Co_9S_8 @MoS_2 catalyst. Mott-Schottky test was also conducted to reveal the electronic interaction. As given in Fig. S6, the positive slopes of MoS_2, Co_9S_8 and Co_9S_8 @MoS_2 samples reflect the typical n-type semiconductor characteristics. In particular, the flat-band potential of the heterostructured Co_9S_8 @MoS_2 exhibits a positive shift, confirming the change of electron distribution between Co_9S_8 and MoS_2.

From the above characterization results, we successfully synthesized heterogeneous catalysts Co_9S_8@MoS_2. The intimate contact between Co_9S_8 and MoS_2 could form heterogeneous interfaces and expose more active sites. Meanwhile, electron redistribution was induced at the heterointerfaces of Co_9S_8 @MoS_2 due to the different electronic structures. The shift of Co/Mo peaks in XPS and change of flat-band potential in Mott-Schottky plots both confirm the strong electronic interaction between Co_9S_8 and MoS_2. The formed heterostructure interfaces prompt electron transfer from Co_9S_8 to MoS_2 [55], which could facilitate the adsorption of oxygen-containing intermediates and promote reaction activity at the Co sites, thus to improve the OER activity.

3.2. Oxygen evolution reaction activity

The OER performance was evaluated by linear scan voltammetry in O_2-saturated KOH aqueous electrolyte. For comparison, PMo_{12} @ZIF-67 sulfurized at different temperatures (denoted as CoMoS-X, X representing the temperature) and PMo_{12} @ZIF-67 precursors sintered in Ar atmosphere without sulfur source (denoted as CoMo-X) were also tested.

As illustrated in Fig. S7, the CoMoS-750 catalyst exhibits the best OER performance among the tested temperature and atmosphere. To reach 10 mA cm^{-2}, the CoMoS-750 only needs the overpotential of 242 mV, compared to 305 mV for CoMoS-500 and 276 mV for CoMoS-850. Besides, the OER activity of the CoMoS-750 is also superior to Ar annealed CoMo-500 and CoMo-750 catalysts. This indicates that the chemical and electronic states of the metal sulfides are critical for their OER activity.

The CoMoS-750 catalyst with the hetero-structure of Co_9S_8 @MoS_2 shows better OER activity comparing to the pure Co_9S_8 and MoS_2, as well as the mechanical mixtures of Co_9S_8 and MoS_2 (named as Co_9S_8 +MoS_2). As depicted in Fig. 6a, the required overpotential at 10 mA cm^{-2} for heterostructured Co_9S_8 @MoS_2 is the smallest value among the tested electrocatalysts, while Co_9S_8, MoS_2 and Co_9S_8 +MoS_2 need larger overpotential of 264, 401 and 297 mV, respectively. The lower overpotential of Co containing catalysts suggests that Co_9S_8 plays a major role for OER process. As for the mixture catalyst Co_9S_8 +MoS_2 by mechanical mixing, the OER activity is lower than that of Co_9S_8 @MoS_2, suggesting that synergetic effect at the Co_9S_8-MoS_2 interfaces is presented in the heterostructure Co_9S_8 @MoS_2 catalyst. The promoted electron transfer from Co_9S_8 to MoS_2 leads to an improved OER activity. As a comparison, the polarization curve of the commercial RuO_2 catalyst was also shown in Fig. 6a with an overpotential of 320 mV. Notably, the Co_9S_8 @MoS_2 outperforms the commercial RuO_2. The OER activities of the catalysts at high current density were also investigated as a consideration for practical application. The required overpotential at 100 mA cm^{-2} for the heterostructured Co_9S_8 @MoS_2 catalyst is 329 mV. Furthermore, the solid supports effect for the OER activity was investigated in Fig. S8. From the figure we can see that Co_9S_8 @MoS_2 shows good catalytic performance on different supports, indicating the universality of this heterogeneous catalyst loaded at various supports.

Tafel plots were further explored to learn the catalytic activity of all
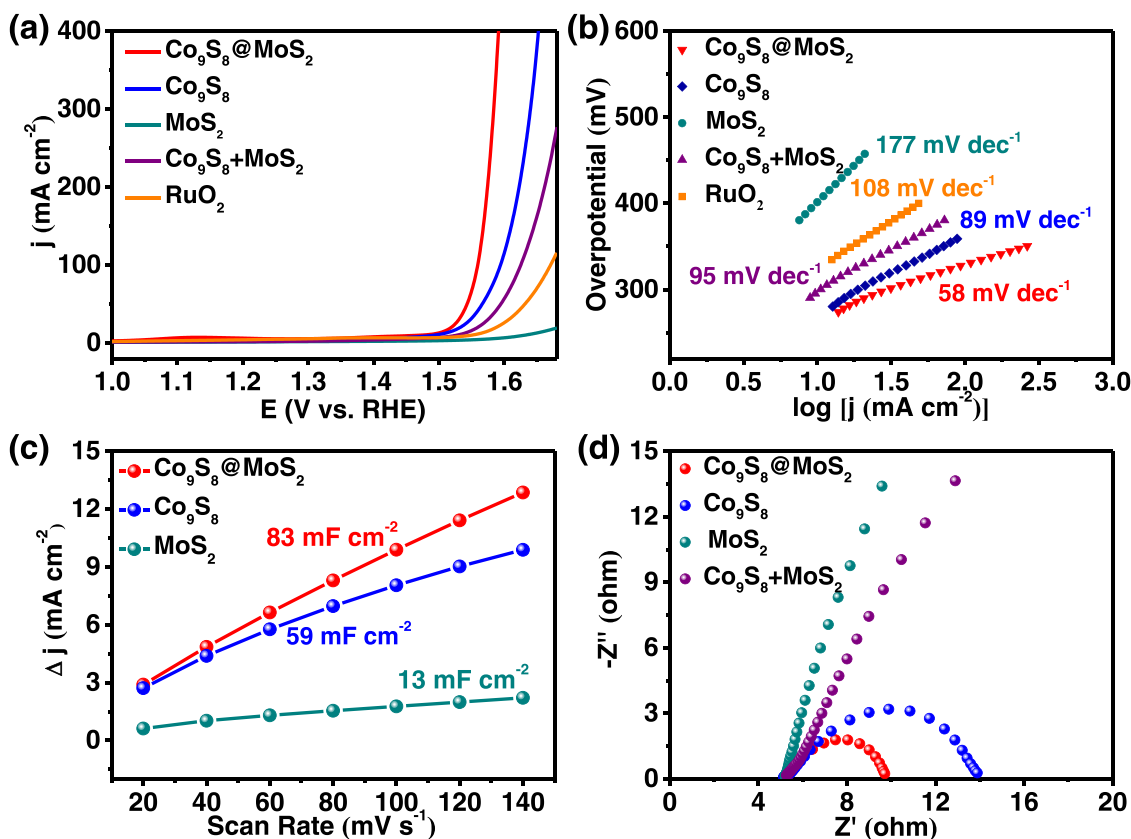

Fig. 6. Electrochemical characterizations of the OER catalysts. (a) OER polarization curves of RuO_2, Co_9S_8, MoS_2, Co_9S_8 @MoS_2 and Co_9S_8 +MoS_2 in O_2-saturated alkaline electrolyte with *IR* compensation. Scan rate: 10 mV s^{-1}. (b) Corresponding Tafel plots for all electrocatalysts. (c) The capacitive current at 1.25 V (vs. RHE) as a function of scan rate for Co_9S_8 @MoS_2, Co_9S_8, MoS_2 (d) Nyquist plots of the Co_9S_8, MoS_2, Co_9S_8 @MoS_2 and Co_9S_8 +MoS_2 at 1.53 V (vs. RHE).

the electrocatalysts. Fig. 6b illustrates that the Co_9S_8 @MoS_2 has the lowest Tafel slope of 58 mV dec^{-1}, compared to that of Co_9S_8 (67 mV dec^{-1}), Co_9S_8 +MoS_2 (95 mV dec^{-1}), MoS_2 (177 mV dec^{-1}) and RuO_2 (108 mV dec^{-1}). The lowest Tafel slope suggests that the Co_9S_8 @MoS_2 has the fastest OER reaction kinetics. Table S1 compares the performances of different other reported OER electrocatalysts under alkaline electrolyte. Our Co_9S_8 @MoS_2 catalyst exhibits outstanding OER activity among the reported transition metal electrocatalysts.

ECSA and EIS measurements were tested to elucidate the outstanding OER activity of Co_9S_8 @MoS_2. ECSA can be obtained by the C_{dl} of the catalysts through CV scans with various scan rates (Fig. S9) [62]. As observed in Fig. 6c, the C_{dl} value of heterostructured Co_9S_8 @MoS_2 is 83 mF cm^{-2}, much higher than that of Co_9S_8 (59 mF cm^{-2}) and MoS_2 (13 mF cm^{-2}). Larger ECSA suggests better contact between the working electrode and electrolyte, thus provides more active sites for OER. In Fig. 6d, EIS characterizations were used to illustrate the OER kinetics of the electrocatalysts. The charge transfer resistance (R_{ct}) is calculated from the size of semicircle in the EIS curves. Smaller semicircle of the Co_9S_8 @MoS_2 catalyst suggests lower electron transfer impedance [63]. The faster electron transfer kinetics should be due to the strong interactions between Co_9S_8 and MoS_2 in the heterostructured catalyst.

DFT calculations were performed on the Co/Mo-sulfide catalyst to understand the synergetic effects and the nature of the outstanding OER activity. Typically, OER undergoes a four-electron step process, thus the absorption energies of oxygen-containing intermediates were calculated. Fig. 7a and b give the side-view of the schematic models for Co_9S_8 (311) and Co_9S_8 (311)-MoS_2 hetero-structures with *OH, *O and *OOH adsorbed on their surfaces. Fig. 7c presents the Gibbs free-energy diagrams. The rate determining step (RDS) for Co_9S_8 (311) is conversion of O* to *OOH at U= 0 V and the energy barrier is 1.93 eV. As for the Co_9S_8 @MoS_2, the surface Co sites at the Co_9S_8 and MoS_2 interfaces had the same RDS with a reduced energy barrier of 1.80 eV. The energy diagrams at U= 1.23 V were shown in Fig. 7d. The largest uphill barrier is 0.70 eV for Co_9S_8 and 0.57 eV for Co_9S_8 @MoS_2. The lower energy barrier of Co sites in the heterostructure indicates that the Co_9S_8 @MoS_2 catalyst is more efficient for electrocatalytic OER with lower overpotential and faster kinetic. This further proves that the electronic interaction between Co_9S_8 and MoS_2 can optimize electronic structure of Co sites, thereby improving the activity of OER.

Long-term durability and stability are also important for practical industrial application. As shown in the chronopotentiometric curve in Fig. S10, the OER activity of Co_9S_8 @MoS_2 has good stability which can maintain stable for 20 h. However, under the high potential of OER process, the transition metal sulfides at the surface of the catalysts evolve through in-situ oxidation reactions to form metal oxides or hydroxides, which are the actual OER active materials [52,64]. Therefore, TEM and XPS were conducted after OER stability test to investigate the conversion of the electrocatalyst. As illustrated in Fig. S11, the MoS_2 nanosheets at the catalyst shell shrink significantly and convert to a thin coating on the catalyst surface. XPS shows that higher metal valence
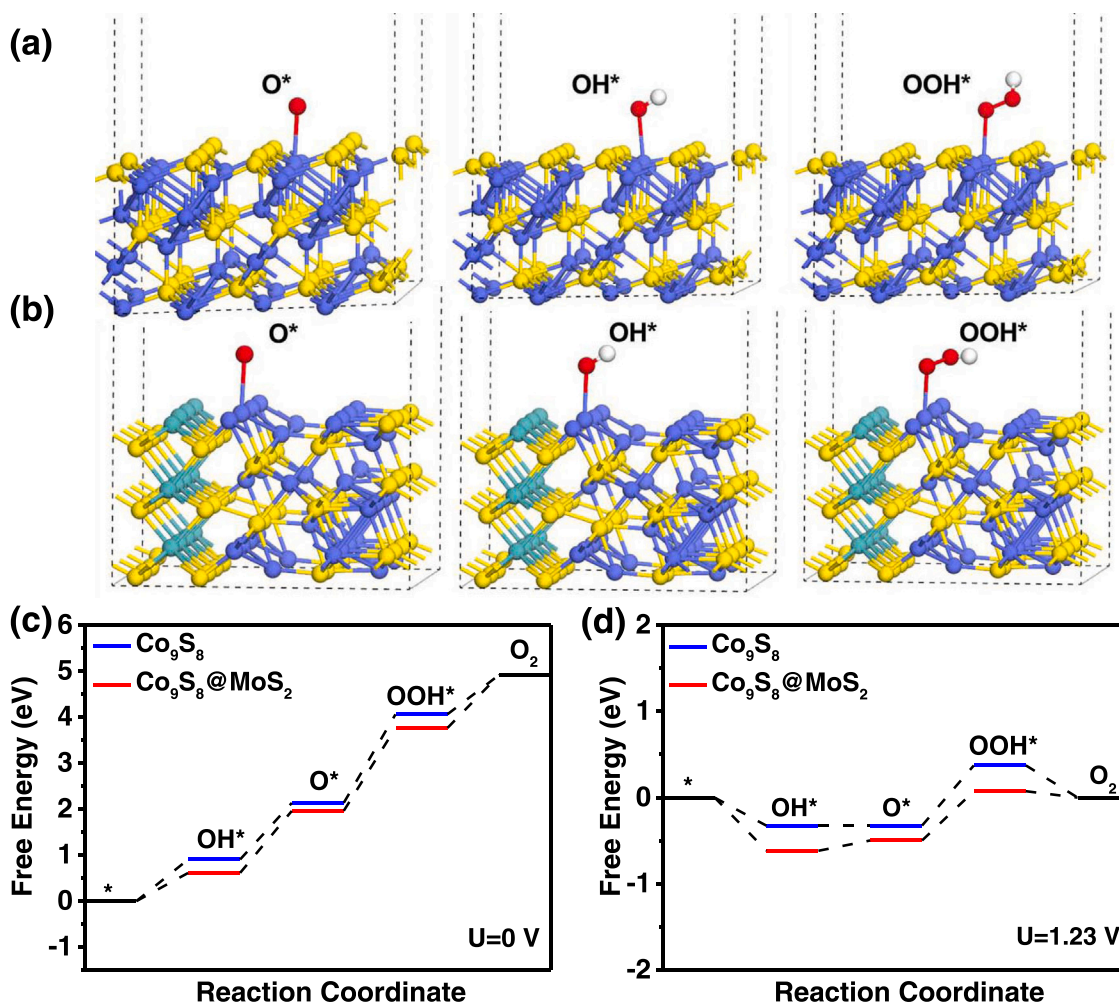

Fig. 7. DFT calculation of the OER intermediates on different catalyst configurations. (a-b) Side-view schematic of the catalysts with *OH, *O, and *OOH intermediates on the surface (a) Co_9S_8 (311) and (b) Co_9S_8 (311)-MoS_2 heterostructures. (c-d) Gibbs free-energy diagram for OER process at 0 V (c) and 1.23 V (d) for the Co_9S_8 and Co_9S_8 @MoS_2 heterostructures. The purple, green, yellow, white and red balls represent cobalt, molybdenum, sulfur, hydrogen and oxygen.

states of Co^{3+} and Mo^{6+} (Fig. S12) increased after OER. The signals of S^{2-} become weaker due to the surface oxidation and at 529.7 eV a new peak of O 1 s arises due to the formation of metal-O bonds [65]. These results suggest that the surface of Co_9S_8 @MoS_2 in the heterostructure undergoes oxidation during the OER reaction, and partially converted into Co (oxo) hydroxide and MoO_3 species.

3.3. Constructing integrated PSC–EC water splitting system

Encouraged by excellent OER activities of heterostructured Co_9S_8 @MoS_2, an overall water splitting setup was established by employing the commercial Pt/C and Co_9S_8 @MoS_2 as cathode and anode, respectively. As illustrated in Fig. 8a, the voltage required at 10 mA cm^{-2} for two-electrode Co_9S_8 @MoS_2/Pt/C is only 1.52 V, outperforming the noble RuO_2//Pt/C system with a voltage of 1.62 V. The two-electrode Co_9S_8 @MoS_2/Pt/C water splitting system also exhibits good stability upon long-term test. As shown in Fig. S13, there is only a slight degradation during the 24 h water splitting test.

PSCs were integrated with the Co_9S_8 @MoS_2//Pt/C cell to construct an unbiased water splitting system. The fabrication and characterization of the monolithic series connected PSCs are provided in the supporting information (Fig. S14). High efficiency triple cations PSCs, with the structure of ITO/SnO_2/perovskite/spiro-OMeTAD/Au, were fabricated. For a single PSC with the area of 0.4 cm^2, the open circuit voltage (V_{OC}) can reach 1.06 V. Fig. S15a demonstrates the J-V curve of PSC. Owing to outstanding OER catalyst, the water splitting system needs only two cells in series to provide enough voltage to drive the electrolysis, significantly reducing the parasitic power loss from solar cell series connection. Under the simulated solar illumination, the series connected PSC yields a power conversion efficiency (PCE) of 17.4% with an V_{OC} of 2.04 V, a

short circuit current density of 11.5 mA cm^{-2} and a fill factor of 73.8% (Fig. 8b). The J-V curve of series connected PSC intersects with polarization curve of the two-electrode Co_9S_8 @MoS_2/Pt/C system at a voltage of 1.52 V and the corresponding current density is 11.1 mA cm^{-2}. The area of electrocatalyst and solar cell are carefully matched to adjust the intersection as close as possible to the maximum power point (MPP) of the PSC (V_{MPP}=1.66 V) [20]. The coulombic efficiency of the EC system is close to unity, resulting in a STH efficiency of 13.6%. The schematic diagram of integrated PSC-EC system for unbiased solar water splitting is shown in Fig. 8c. The electrochemical workstation is connected in series to record the current and PSCs are used as external power to drive water splitting. The I–t curve of the integrated PSC-EC system for unbiased water splitting was measured under chopped illuminations. As shown in Fig. 8d, when the PSCs are illuminated, the photocurrent generated by PSCs to drive water splitting is 10.6 mA cm^{-2}; this value corresponds to the STH efficiency of 13.0%. The efficiency loss compared with the J-V intersection point in Fig. 8b is due to the contact resistance of conducting wires and J-V hysteresis of the PSCs. The stable output of PSCs is slightly lower than the maximum power point measured in reversed J-V scan. The J-V hysteresis of PSCs is given in Fig. S15b. The photocurrent drops to zero when the light is turned off, indicating that the PSCs provides the external voltage to drive the electrochemical reaction under light. The small delay of photocurrent under light condition is due to the light soaking effect of the solar cell, which can be circumvented by reducing the J-V hysteresis of the PSCs. Stability of the PSC-EC system was tested for 2 h under continuous illumination. The STH efficiency is relatively stable with a slight decrease of photocurrent to 87% of its initial value (Fig. S16). Encapsulation of the PSCs could further improve the long term stability of the PSC-EC water splitting system.
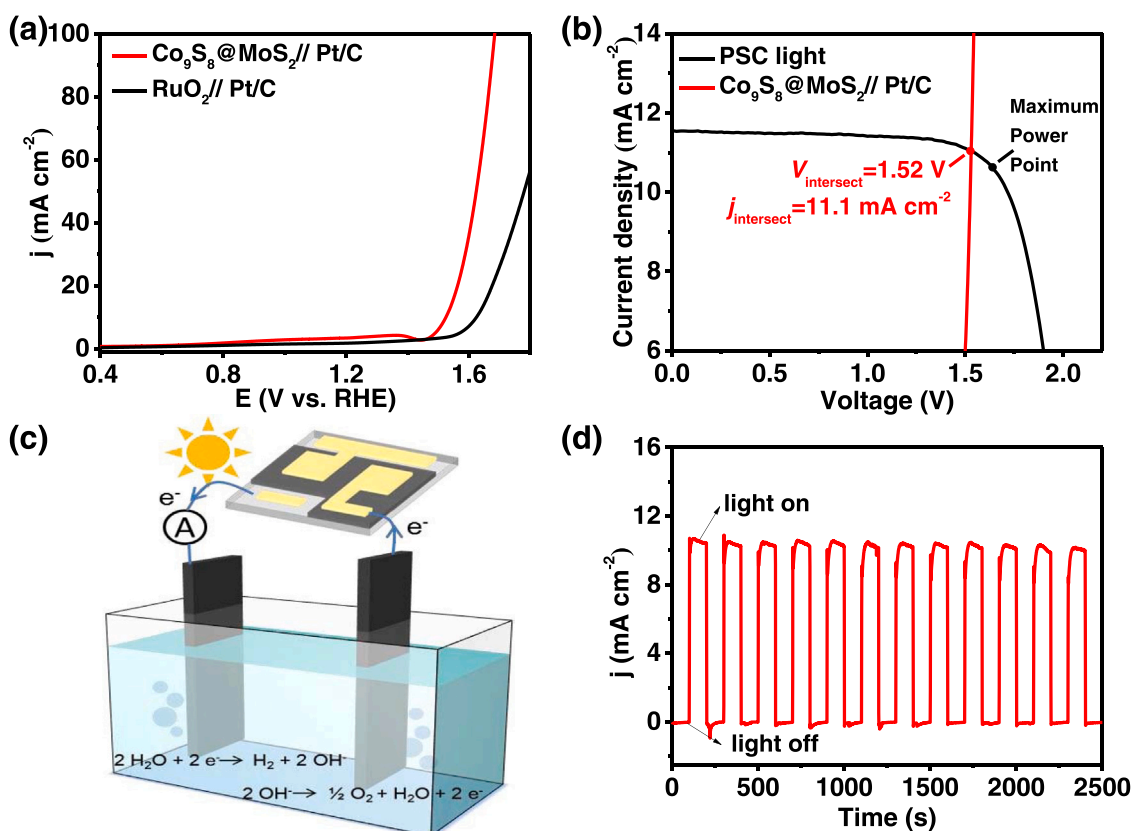
Fig. 8. Performance of PSC-EC unbiased solar water splitting system. (a) Polarization curves of Co_9S_8 @MoS_2/Pt/C and RuO_2//Pt/C for two-electrode water splitting. Scan rate: 10 mV s^{-1}. (b) The interaction of J–V curves for the Co_9S_8 @MoS_2/Pt/C EC system and the series connected PSCs under illumination of simulated AM 1.5 G (100 mW cm^{-2}). (c) Schematic diagram of integrated PSC-EC system for water splitting. (d) I-t curves of the integrated PSC-EC unbiased water splitting system under illumination of chopped simulated AM 1.5 G (100 mW cm^{-2}) at 0 V vs the Pt/C counter electrode.

4. Conclusions

In summary, we have synthesized a highly efficient Co_9S_8 @MoS_2 heterostructure OER catalyst by controlling the sulfurization process on the PMo_{12}-embedded ZIF-67 precursor. The as-obtained Co_9S_8 @MoS_2 catalyst shows excellent OER activity and stability, outperforming RuO_2 and most of the non-noble electrocatalysts. This is due to the construction of synergetic interfaces that induce strong electronic interaction between Co_9S_8 and MoS_2. Finally, a two-electrode Co_9S_8 @MoS_2//Pt/C cell is integrated with PSCs to construct an unbiased water splitting system, which could yield a high STH efficiency of 13.6%. This study presents a new approach for enhancing electrocatalytic activity of Co-based OER catalysts and thereafter constructing unbiased PSC-EC water splitting system for efficient utilization of solar energy.

CRediT authorship contribution statement

Meng Wang: Investigation, Writing – original draft. **Zhi Wan:** Investigation, Writing – review & editing. **Xinying Meng, Zhihao Li, Xiaogang Ding** and **Pan Li:** Assist in experimental tests. **Can Li:** review & editing. **Jian-Gan Wang** and **Zhen Li:** Conceptualization, Supervision, Writing – review & editing, Funding acquisition.

Declaration of Competing Interest

The authors declare that they have no known competing financial interests or personal relationships that could have appeared to influence the work reported in this paper.

Appendix A. Supporting information

Supplementary data associated with this article can be found in the online version at doi:10.1016/j.apcatb.2022.121272.

References

[1] D. Shindell, C.J. Smith, Climate and air-quality benefits of a realistic phase-out of fossil fuels (https://doi:), Nature 573 (2019) 408–411, https://doi.org/10.1038/s41586-019-1554-z.

[2] A. Zhang, Y. Liang, H. Zhang, Z. Geng, J. Zeng, Doping regulation in transition metal compounds for electrocatalysis (https://doi:), Chem. Soc. Rev. 50 (2021) 9817–9844, https://doi.org/10.1039/D1CS00330E.

[3] J.A. Turner, Sustainable hydrogen production (https://doi:), Science 305 (2004) 972–974, https://doi.org/10.1126/science.1103197.

[4] M.S. Dresselhaus, I.L. Thomas, Alternative energy technologies (https://doi:), Nature 414 (2001) 332–337, https://doi.org/10.1038/35104599.

[5] S.S. Lam, V.-H. Nguyen, M.T. Nguyen Dinh, D.Q. Khieu, D.D. La, H.T. Nguyen, D.V. N. Vo, C. Xia, R.S. Varma, M. Shokouhimehr, C.C. Nguyen, Q.V. Le, W. Peng, Mainstream avenues for boosting graphitic carbon nitride efficiency: towards enhanced solar light-driven photocatalytic hydrogen production and environmental remediation (https://doi:), J. Mater. Chem. A 8 (2020) 10571–10603, https://doi.org/10.1039/d0ta02582h.

[6] V.-H. Nguyen, H.H. Do, T. Van Nguyen, P. Singh, P. Raizada, A. Sharma, S.S. Sana, A.N. Grace, M. Shokouhimehr, S.H. Ahn, C. Xia, S.Y. Kim, Q.V. Le, Perovskite oxide-based photocatalysts for solar-driven hydrogen production: progress and perspectives (https://doi:), Sol. Energy 211 (2020) 584–599, https://doi.org/10.1016/j.solener.2020.09.078.

[7] O. Khaselev, J.A. Turner, A monolithic photovoltaic-photoelectrochemical device for hydrogen production via water splitting (https://doi:), Science 280 (1998) 425–427, https://doi.org/10.1126/science.280.5362.425.

[8] M.G. Walter, E.L. Warren, J.R. McKone, S.W. Boettcher, Q. Mi, E.A. Santori, N. S. Lewis, Solar water splitting cells (https://doi:), Chem. Rev. 110 (2010) 6446–6473, https://doi.org/10.1021/cr1002326.

[9] S. Esiner, H. van Eersel, G.W.P. van Pruissen, M. Turbiez, M.M. Wienk, R.A. J. Janssen, Water splitting with series-connected polymer solar cells (https://doi:), ACS Appl. Mater. Inter. 8 (2016) 26972–26981, https://doi.org/10.1021/acsami.6b06381.

[10] J.-W. Schüttauf, M.A. Modestino, E. Chinello, D. Lambelet, A. Delfino, D. Dominé, A. Faes, M. Despeisse, J. Bailat, D. Psaltis, C. Moser, C. Ballif, Solar-to-hydrogen production at 14.2% efficiency with silicon photovoltaics and earth-abundant electrocatalysts (https://doi:), J. Electrochem. Soc. 163 (2016) F1177–F1181, https://doi.org/10.1149/2.0541610jes.

[11] F. Zhou, R. Sa, X. Zhang, S. Zhang, Z. Wen, R. Wang, Robust ruthenium diphosphide nanoparticles for pH-universal hydrogen evolution reaction with platinum-like activity, Appl. Cat. B Environ. 274 (2020), 119092, https://doi.org/10.1016/j.apcatb.2020.119092.

[12] Y. Jiao, Y. Zheng, M. Jaroniec, S.Z. Qiao, Design of electrocatalysts for oxygen- and hydrogen-involving energy conversion reactions (https://doi:), Chem. Soc. Rev. 44 (2015) 2060–2086, https://doi.org/10.1039/C4CS00470A.

[13] G.H. Han, H. Kim, J. Kim, J. Kim, S.Y. Kim, S.H. Ahn, Micro-nanoporous MoO2@ CoMo heterostructure catalyst for hydrogen evolution reaction, Appl. Catal. B Environ. 270 (2020), 118895, https://doi.org/10.1016/j.apcatb.2020.118895.

[14] W. Li, C. Wang, X. Lu, Integrated transition metal and compounds with carbon nanomaterials for electrochemical water splitting (https://doi:), J. Mater. Chem. A 9 (2021) 3786–3827, https://doi.org/10.1039/D0TA09495A.

[15] X. Gu, Z. Liu, M. Li, J. Tian, L. Feng, Surface structure regulation and evaluation of FeNi-based nanoparticles for oxygen evolution reaction, Appl. Catal. B Environ. 297 (2021), 120462, https://doi.org/10.1016/j.apcatb.2021.120462.

[16] J. Wang, F. Xu, H. Jin, Y. Chen, Y. Wang, Non-noble metal-based carbon composites in hydrogen evolution reaction: fundamentals to applications (https://doi:), Adv. Mater. 29 (2017), 1605838, https://doi.org/10.1002/adma.201605838.

[17] B. Zhang, F. Yang, X. Liu, N. Wu, S. Che, Y. Li, Phosphorus doped nickel-molybdenum aerogel for efficient overall water splitting, Appl. Catal. B Environ. 298 (2021), 120494, https://doi.org/10.1016/j.apcatb.2021.120494.

[18] N. Li, X. Niu, Q. Chen, H. Zhou, Towards commercialization: the operational stability of perovskite solar cells (https:// doi:), Chem. Soc. Rev. 49 (2020) 8235–8286, https://doi.org/10.1039/D0CS00573H.

[19] Z. Li, T.R. Klein, D.H. Kim, M. Yang, J.J. Berry, M.F.A.M. van Hest, K. Zhu, Scalable fabrication of perovskite solar cells (https://doi:), Nat. Rev. Mater. 3 (2018) 18017, https://doi.org/10.1038/natrevmats.2018.17.

[20] J.S. Luo, J.H. Im, M.T. Mayer, M. Schreier, M.K. Nazeeruddin, N.G. Park, S. D. Tilley, H.J. Fan, M. Gratzel, Water photolysis at 12.3% efficiency via perovskite photovoltaics and Earth-abundant catalysts (https://doi:), Science 345 (2014) 1593–1596, https://doi.org/10.1126/science.1258307.

[21] H. Roh, H. Jung, H. Choi, J.W. Han, T. Park, S. Kim, K. Yong, Various metal (Fe, Mo, V, Co)-doped Ni2P nanowire arrays as overall water splitting electrocatalysts and their applications in unassisted solar hydrogen production with STH 14%, Appl. Catal. B Environ. 297 (2021) 120434 https://doi.org/10.1016/j.apcatb.2021.120434.

[22] W. Yang, J. Park, H.-C. Kwon, O.S. Hutter, L.J. Phillips, J. Tan, H. Lee, J. Lee, S. D. Tilley, J.D. Major, J. Moon, Solar water splitting exceeding 10% efficiency via low-cost Sb2Se3 photocathodes coupled with semitransparent perovskite photovoltaics (https://doi:), Energy Environ. Sci. 13 (2020) 4362–4370, https://doi.org/10.1039/D0EE02959A.

[23] J. Luo, Z. Li, S. Nishiwaki, M. Schreier, M.T. Mayer, P. Cendula, Y.H. Lee, K. Fu, A. Cao, M.K. Nazeeruddin, Y.E. Romanyuk, S. Buecheler, S.D. Tilley, L.H. Wong, A. N. Tiwari, M. Grätzel, Targeting ideal dual-absorber tandem water splitting using perovskite photovoltaics and CuInxGa1-xSe2 photocathodes, Adv. Energy Mater. 5 (2015), 1501520, https://doi.org/10.1002/aenm.201501520.

[24] B. Fei, Z. Chen, Y. Ha, R. Wang, H. Yang, H. Xu, R. Wu, Anion-cation co-substitution activation of spinel CoMoO4 for efficient oxygen evolution reaction, Chem. Eng. J. 394 (2020) 124926, https://doi.org/10.1016/j.cej.2020.124926.

[25] Z.-X. Shi, J.-W. Zhao, C.-F. Li, H. Xu, G.-R. Li, Fully exposed edge/corner active sites in Fe substituted-Ni(OH)2 tube-in-tube arrays for efficient electrocatalytic oxygen evolution, Appl. Catal. B Environ. 298 (2021) 120558, https://doi.org/10.1016/j.apcatb.2021.120558.

[26] S. Yin, W. Tu, Y. Sheng, Y. Du, M. Kraft, A. Borgna, R. Xu, A highly efficient oxygen evolution catalyst consisting of interconnected nickel-iron-layered double hydroxide and carbon nanodomains (https://doi:), Adv. Mater. 30 (2018), https://doi.org/10.1002/adma.201705106.

[27] M. Xie, X. Xiong, L. Yang, X. Shi, A.M. Asiri, X. Sun, An Fe(TCNQ)2 nanowire array on Fe foil: an efficient non-noble-metal catalyst for the oxygen evolution reaction in alkaline media (https://doi:), Chem. Commun. 54 (2018) 2300–2303, https://doi.org/10.1039/c7cc09105b.

[28] X. Liu, Y. Wang, L. Chen, P. Chen, S. Jia, Y. Zhang, S. Zhou, J. Zang, Co2B and Co nanoparticles immobilized on the N–B-doped carbon derived from nano-B4C for efficient catalysis of oxygen evolution, hydrogen evolution, and oxygen reduction reactions (https://doi:), ACS Appl. Mater. Inter. 10 (2018) 37067–37078, https://doi.org/10.1021/acsami.8b13359.

[29] Q. Liu, J. Zhang, A general and controllable synthesis of ComSn (Co9S8, Co3S4, and Co1−xS) hierarchical microspheres with homogeneous phases (https://doi:), CrystEngComm 15 (2013) 5087–5092, https://doi.org/10.1039/C3CE40251G.

[30] H. Kim, J. Park, I. Park, K. Jin, S.E. Jerng, S.H. Kim, K.T. Nam, K. Kang, Coordination tuning of cobalt phosphates towards efficient water oxidation

catalyst (https://doi:), Nat. Commun. 6 (2015) 8253, https://doi.org/10.1038/ncomms9253.

[31] M.-I. Jamesh, M. Harb, Tuning the electronic structure of the earth-abundant electrocatalysts for oxygen evolution reaction (OER) to achieve efficient alkaline water splitting – A review (https://doi:), J. Energy Chem. 56 (2021) 299–342, https://doi.org/10.1016/j.jechem.2020.08.001.

[32] J. Peng, X. Chen, W.-J. Ong, X. Zhao, N. Li, Surface and heterointerface engineering of 2D MXenes and their nanocomposites: insights into electro- and photocatalysis (https://doi:), Chem 5 (2019) 18–50, https://doi.org/10.1016/j.chempr.2018.08.037.

[33] G. Zhao, P. Li, N. Cheng, S.X. Dou, W. Sun, An Ir/Ni(OH)2 heterostructured electrocatalyst for the oxygen evolution reaction: breaking the scaling relation, stabilizing iridium(v), and beyond, Adv. Mater. 32 (2020), 2000872, https://doi.org/10.1002/adma.202000872.

[34] J. Nai, X. Xu, Q. Xie, G. Lu, Y. Wang, D. Luan, X. Tao, X.W. Lou, Construction of Ni (CN)2/NiSe2 heterostructures by stepwise topochemical pathways for efficient electrocatalytic oxygen evolution, Adv. Mater. 34 (2022), 2104405, https://doi.org/10.1002/adma.202104405.

[35] G. Zhao, K. Rui, S.X. Dou, W. Sun, Heterostructures for electrochemical hydrogen evolution reaction: a review, Adv. Funct. Mater. 28 (2018), 1803291, https://doi.org/10.1002/adfm.201803291.

[36] L. Yang, W. Zhou, D. Hou, K. Zhou, G. Li, Z. Tang, L. Li, S. Chen, Porous metallic MoO2-supported MoS2 nanosheets for enhanced electrocatalytic activity in the hydrogen evolution reaction (https://doi:), Nanoscale 7 (2015) 5203–5208, https://doi.org/10.1039/C4NR06754A.

[37] Y. Arafat, M.R. Azhar, Y.J. Zhong, H.R. Abid, M.O. Tade, Z.P. Shao, Advances in zeolite imidazolate frameworks (ZIFs) derived bifunctional oxygen electrocatalysts and their application in zinc-air batteries (https://doi:), Adv. Energy Mater. 11 (2021) 56, https://doi.org/10.1002/aenm.202100514.

[38] J. He, Z. Hu, J. Zhao, P. Liu, X. Lv, W. Tian, C. Wang, S. Tan, J. Ji, Ni-decorated Fe-/N- co-doped carbon anchored on porous cobalt oxide nanowires arrays for efficient electrocatalytic oxygen evolution (https://doi:), Chem. Eng. Sci. 243 (2021), 116774, https://doi.org/10.1016/j.ces.2021.116774.

[39] Z. Chen, S. Chen, S. Siahrostami, P. Chakthranont, C. Hahn, D. Nordlund, S. Dimosthenis, J.K. Nørskov, Z. Bao, T.F. Jaramillo, Development of a reactor with carbon catalysts for modular-scale, low-cost electrochemical generation of H2O2 (https://doi:), Reac. Chem. Eng. 2 (2017) 239–245, https://doi.org/10.1039/C6RE00195E.

[40] H.H. Do, Q.V. Le, T.V. Nguyen, K.A. Huynh, M.A. Tekalgne, V.A. Tran, T.H. Lee, J. H. Cho, M. Shokouhimehr, S.H. Ahn, H.W. Jang, S.Y. Kim, Synthesis of MoSx/Ni-metal-organic framework-74 composites as efficient electrocatalysts for hydrogen evolution reactions (https://doi:), Int. J. Energy Res. 45 (2021) 9638–9647, https://doi.org/10.1002/er.6385.

[41] K. Zhang, K.O. Kirlikovali, R.S. Varma, Z. Jin, H.W. Jang, O.K. Farha, M. Shokouhimehr, Covalent organic frameworks: emerging organic solid materials for energy and electrochemical applications (https://doi:), ACS Appl. Mater. Inter. 12 (2020) 27821–27852, https://doi.org/10.1021/acsami.0c06267.

[42] N. Zaman, T. Noor, N. Iqbal, Recent advances in the metal–organic framework-based electrocatalysts for the hydrogen evolution reaction in water splitting: a review (https://doi:), RSC Adv. 11 (2021) 21904–21925, https://doi.org/10.1039/d1ra02240g.

[43] C. Xia, K.O. Kirlikovali, T.H.C. Nguyen, X.C. Nguyen, Q.B. Tran, M.K. Duong, M. T. Nguyen Dinh, D.L.T. Nguyen, P. Singh, P. Raizada, V.-H. Nguyen, S.Y. Kim, L. Singh, C.C. Nguyen, M. Shokouhimehr, Q.V. Le, The emerging covalent organic frameworks (COFs) for solar-driven fuels production, Coord. Chem. Rev. 446 (2021), 214117 https://doi.org/10.1016/j.ccr.2021.214117.

[44] J. Li, S. Zou, X. Liu, Y. Lu, D. Dong, Electronically modulated CoP by Ce doping as a highly efficient electrocatalyst for water splitting (https://doi:), ACS Sustain. Chem. Eng. 8 (2020) 10009–10016, https://doi.org/10.1021/acssuschemeng.0c01193.

[45] S. Dilpazir, P. Ren, R. Liu, M. Yuan, M. Imran, Z. Liu, Y. Xie, H. Zhao, Y. Yang, X. Wang, C. Streb, G. Zhang, Efficient tetra-functional electrocatalyst with synergetic effect of different active sites for multi-model energy conversion and storage (https://doi:), ACS Appl. Mater. Inter. 12 (2020) 23017–23027, https://doi.org/10.1021/acsami.0c05481.

[46] B.Y. Guan, Y. Lu, Y. Wang, M. Wu, X.W. Lou, Porous iron–cobalt alloy/nitrogen-doped carbon cages synthesized via pyrolysis of complex metal–organic framework hybrids for oxygen reduction (https://doi:), Adv. Funct. Mater. 28 (2018), 1706738, https://doi.org/10.1002/adfm.201706738.

[47] Z. Yu, Y. Bai, Y. Liu, S. Zhang, D. Chen, N. Zhang, K. Sun, Metal–organic-framework-derived yolk–shell-structured cobalt-based bimetallic oxide polyhedron

[48] J.J. Walsh, A.M. Bond, R.J. Forster, T.E. Keyes, Hybrid polyoxometalate materials for photo(electro-) chemical applications, Coord. Chem. Rev. 306 (2016) 217–234, https://doi.org/10.1016/j.ccr.2015.06.016.

[49] K.S. Park, Z. Ni, A.P. Côté, J.Y. Choi, R. Huang, F.J. Uribe-Romo, H.K. Chae, M. O'Keeffe, O.M. Yaghi, Exceptional chemical and thermal stability of zeolitic imidazolate frameworks (https://doi:), Proc. Natl. Acad. Sci. 103 (2006) 10186–10191, https://doi.org/10.1073/pnas.0602439103.

[50] Y. Wang, R. Dong, P. Tan, H. Liu, H. Liao, M. Jiang, Y. Liu, L. Yang, J. Pan, Investigating the active sites in molybdenum anchored nitrogen-doped carbon for alkaline oxygen evolution reaction, J. Colloid Interf. Sci. 609 (2022) 617–626, https://doi.org/10.1016/j.jcis.2021.11.058.

[51] L. Zhang, T. Mi, M.A. Ziaee, L. Liang, R. Wang, Hollow POM@MOF hybrid-derived porous Co3O4/CoMoO4 nanocages for enhanced electrocatalytic water oxidation (https://doi:), J. Mater. Chem. A 6 (2018) 1639–1647, https://doi.org/10.1039/C7TA08683K.

[52] C.-C. Hou, L. Zou, Y. Wang, Q. Xu, MOF-mediated fabrication of a porous 3D superstructure of carbon nanosheets decorated with ultrafine cobalt phosphide nanoparticles for efficient electrocatalysis and zinc–air batteries, Angew. Chem. Int. Ed. 59 (2020) 21360–21366, https://doi.org/10.1002/anie.202011347.

[53] A.G. Abd-Elrahim, D.-M. Chun, Nanosized Co3O4–MoS2 heterostructure electrodes for improving the oxygen evolution reaction in an alkaline medium, J. Alloy. Compd. 853 (2021), 156946, https://doi.org/10.1016/j.jallcom.2020.156946.

[54] M. Kim, M.A.R. Anjum, M. Choi, H.Y. Jeong, S.H. Choi, N. Park, J.S. Lee, Covalent 0D–2D heterostructuring of Co9S8–MoS2 for enhanced hydrogen evolution in All pH electrolytes, Adv. Funct. Mater. 30 (2020), 2002536, https://doi.org/10.1002/adfm.202002536.

[55] J. Bai, T. Meng, D. Guo, S. Wang, B. Mao, M. Cao, Co9S8@MoS2 core–shell heterostructures as trifunctional electrocatalysts for overall water splitting and Zn–air batteries (https://doi:), ACS Appl. Mater. Inter. 10 (2018) 1678–1689, https://doi.org/10.1021/acsami.7b14997.

[56] J. Yang, G. Zhu, Y. Liu, J. Xia, Z. Ji, X. Shen, S. Wu, Fe3O4-decorated Co9S8 nanoparticles in situ grown on reduced graphene oxide: a new and efficient electrocatalyst for oxygen evolution reaction, Adv. Funct. Mater. 26 (2016) 4712–4721, https://doi.org/10.1002/adfm.201600674.

[57] Y. Yang, H. Yao, Z. Yu, S.M. Islam, H. He, M. Yuan, Y. Yue, K. Xu, W. Hao, G. Sun, H. Li, S. Ma, P. Zapol, M.G. Kanatzidis, Hierarchical nanoassembly of MoS2/Co9S8/Ni3S2/Ni as a highly efficient electrocatalyst for overall water splitting in a wide pH range (https://doi:), J. Am. Chem. Soc. 141 (2019) 10417–10430, https://doi.org/10.1021/jacs.9b04492.

[58] M. Yuan, S. Dipazir, M. Wang, Y. Sun, D. Gao, Y. Bai, M. Zhang, P. Lu, H. He, X. Zhu, S. Li, Z. Liu, Z. Luo, G. Zhang, Polyoxometalate-assisted formation of CoSe/MoSe2 heterostructures with enhanced oxygen evolution activity (https://doi:), J. Mater. Chem. A 7 (2019) 3317–3326, https://doi.org/10.1039/C8TA11976G.

[59] B. Zhang, X. Zhang, D. Huang, S. Li, H. Yuan, M. Wang, Y. Shen, Co9S8 hollow spheres for enhanced electrochemical detection of hydrogen peroxide, Talanta 141 (2015) 73–79, https://doi.org/10.1016/j.talanta.2015.03.048.

[60] J. Shao, T. Gao, Q. Qu, Q. Shi, Z. Zuo, H. Zheng, Ultrafast Li-storage of MoS2 nanosheets grown on metal-organic framework-derived microporous nitrogen-doped carbon dodecahedrons, J. Power Sources 324 (2016) 1–7, https://doi.org/10.1016/j.jpowsour.2016.05.056.

[61] J. Hou, B. Zhang, Z. Li, S. Cao, Y. Sun, Y. Wu, Z. Gao, L. Sun, Vertically aligned oxygenated-CoS2–MoS2 heteronanosheet architecture from polyoxometalate for efficient and stable overall water splitting (https://doi:), ACS Catal. 8 (2018) 4612–4621, https://doi.org/10.1021/acscatal.8b00668.

[62] L. Yu, H. Zhou, J. Sun, F. Qin, F. Yu, J. Bao, Y. Yu, S. Chen, Z. Ren, Cu nanowires shelled with NiFe layered double hydroxide nanosheets as bifunctional electrocatalysts for overall water splitting (https://doi:), Energy Environ. Sci. 10 (2017) 1820–1827, https://doi.org/10.1039/c7ee01571b.

[63] H. Zhou, F. Yu, J. Sun, H. Zhu, I.K. Mishra, S. Chen, Z. Ren, Highly efficient hydrogen evolution from edge-oriented WS2(1–x)Se2x particles on three-dimensional porous NiSe2 foam (https://doi:), Nano Lett. 16 (2016) 7604–7609, https://doi.org/10.1021/acs.nanolett.6b03467.

[64] J. Zhang, T. Wang, D. Pohl, B. Rellinghaus, R. Dong, S. Liu, X. Zhuang, X. Feng, Interface engineering of MoS2/Ni3S2 heterostructures for highly enhanced electrochemical overall-water-splitting activity, Angew. Chem. Int. Ed. 55 (2016) 6702–6707, https://doi.org/10.1002/anie.201602237.

[65] N. Yao, R. Meng, F. Wu, Z. Fan, G. Cheng, W. Luo, Oxygen-vacancy-induced CeO2/Co4N heterostructures toward enhanced pH-universal hydrogen evolution reactions, Appl. Catal. B Environ. 277 (2020), 119282, https://doi.org/10.1016/j.apcatb.2020.119282.